

Article

Not peer-reviewed version

# Synergistic Effect of He for the Fabrication of Ne and Ar Gas-Charged Silicon Thin Films as Solid Targets for Spectroscopic Studies

[Asunción Fernández](#)\*, [Vanda Godinho](#), [José Avila](#), [Maria Carmen Jiménez de Haro](#), Dirk Hufschmidt, Jennifer López-Viejobueno, Gabriel Eduardo Almanza-Vergara, Francisco Javier Ferrer, [Julien L. Colaux](#), [Stéphane Lucas](#), [Maria C. Asensio](#)

Posted Date: 19 March 2024

doi: 10.20944/preprints202403.1172.v1

Keywords: magnetron sputtering; gas-charged Si films; microstructural characterization; IBA analysis; XPS and XAS spectroscopic analyses; Ne, Ar and He solid targets



Preprints.org is a free multidiscipline platform providing preprint service that is dedicated to making early versions of research outputs permanently available and citable. Preprints posted at Preprints.org appear in Web of Science, Crossref, Google Scholar, Scilit, Europe PMC.

Copyright: This is an open access article distributed under the Creative Commons Attribution License which permits unrestricted use, distribution, and reproduction in any medium, provided the original work is properly cited.

*Article*

# Synergistic Effect of He for the Fabrication of Ne and Ar Gas-Charged Silicon Thin Films as Solid Targets for Spectroscopic Studies

Asunción Fernández <sup>1,\*</sup>, Vanda Godinho <sup>1</sup>, José Ávila <sup>2</sup>, M. Carmen Jiménez de Haro <sup>1</sup>, Dirk Hufschmidt <sup>1</sup>, Jennifer López-Viejobueno <sup>1</sup>, G.Eduardo Almanza-Vergara <sup>1</sup>, F.Javier Ferrer <sup>3</sup>, Julian L. Colaux <sup>4</sup>, Stephane Lucas <sup>4</sup> and M. Carmen Asensio <sup>2,5</sup>

<sup>1</sup> Instituto de Ciencia de Materiales de Sevilla (CSIC-Univ. Sevilla), Avda. Américo Vespucio 49, 41092-Sevilla, Spain.

<sup>2</sup> Synchrotron SOLEIL and Université Paris-Saclay, L'Orme des Merisiers, BP48, 91190 Saint-Aubin, France.

<sup>3</sup> Centro Nacional de Aceleradores (Univ. Sevilla, J. Andalucía, CSIC), Av. Tomas Alva Edison 7, 41092, Sevilla, Spain.

<sup>4</sup> Laboratoire d'Analyse par Réactions Nucléaires (LARN), Namur Institute of Structured Matter (NISM), University of Namur, 61 Rue de Bruxelles, 5000 Namur, Belgium.

<sup>5</sup> Madrid Institute of Materials Science (ICMM), CSIC, Cantoblanco, E-28049 Madrid, Spain.

\* Correspondence: asuncion@icmse.csic.es

**Abstract:** Sputtering of silicon in a Helium magnetron discharge (MS) has been reported as a bottom-up procedure to obtain He-charged silicon films (i.e. He nanobubbles encapsulated in a silicon matrix). The incorporation of heavier noble gases is demonstrated in this work with a synergistic effect producing increased Ne and Ar incorporations when using He-Ne and He-Ar gas mixtures in the MS process. Microstructural and chemical characterizations are reported by ion beam analysis (IBA) and scanning and transmission electron microscopies (SEM and TEM). In addition to gas incorporation, helium promotes the formation of larger nanobubbles. For the case of Ne high resolution X-ray photoelectron and absorption spectroscopies (XPS and XAS) are reported with remarkable dependence of the Ne 1s photoemission and the Ne K-edge absorption on the nanobubbles size and composition. The gas (He, Ne, Ar) charged thin films are proposed as “solid” targets for the characterization of spectroscopic properties of noble gases in a confined state without the need for cryogenics or high-pressure anvils devices. Also their use as targets for nuclear reaction studies is foreseen.

**Keywords:** magnetron sputtering; gas-charged Si films; microstructural characterization; IBA analysis; XPS and XAS spectroscopic analyses; Ne; Ar and He solid targets

## 1. Introduction

The dominating feature of inert gas atoms implanted in most solids by ion beam irradiation over a wide energy range (500 keV-100eV), is their high heat of solution, leading to an essentially zero solubility and gas-atom precipitation (formation of small “bubbles”) [1–6]. Helium has been particularly investigated due to its technological interest to study damage in nuclear reactor materials [7,8]. The implantation of other noble gases such as Ne, Ar and Xe has been also investigated [9–11] showing accumulation of gas trapped in bubbles. Implantation studies refer to a “top-down” methodology with interest to study materials’ degradation in nuclear reactors [7,8] and defect engineering in electronic devices development [12,13]. More recently several works investigated the “bottom-up” magnetron sputtering (MS) deposition in Helium plasmas leading to the tailored fabrication of nanostructured carbon films [14], nanoporous Al [15] or He-charged films [16,17].

In particular films fabricated by MS with formation of nanopores or nanobubbles (He filled nanopores) are attracting growing interest in new materials and applications [17–23]. These include, among others, optical devices [19], electrodes in batteries [20,21] or catalysts [23]. An exhaustive microstructural characterization also showed that gas content and nanobubbles size and shape are finely tunable [17,24,25]. Due to the high density and pressure of He trapped in the nanobubbles [24–27], the He-charged Si films have been proposed as “solid-targets” for nuclear reaction studies in our previous works [28–33].

Building on this background, the first goal of the present work was to evaluate the incorporation of heavier noble gases as Ar and Ne during MS deposition of silicon films. The pure argon MS process has been widely investigated due to relatively high Ar abundance and its high sputtering yield [34]. Argon incorporation has been reported for different film compositions showing modification of mechanical or electrical properties [35,36] and bubbles formation [37]. Previous works also investigated the use of Ar-He gas mixtures for deposition of Ti [16,18] and C [14], in which Ar partial pressure enabled a high sputtering rate to be maintained. In reference [15] Al films were also deposited with different Ar-He gas mixtures. However, only He incorporation was reported in these previous works. In another work [38], including a growth model, we report that the chemical nature of the sputter gas not only affects the sputtering mechanism of the Si target, but also the film growth mechanism. In particular, helium introduces a degree of mobility resulting in the coarsening of small pores [38]. For the use of Ne and Ne-He mixtures in MS deposition, the main results relate to films deposition rates and properties [39–41]. A controlled incorporation of Ne and Ar has also been reported during High Power Impulse MS deposition in Ar-Ne gas mixtures [42]. Investigated matrix materials included vanadium [39], carbon [40,41] and tungsten [42].

The work presented in this article goes further from this previous knowledge and aims to increase Ne and Ar content in gas charged silicon films. A synergistic effect is demonstrated, showing that adding He to the plasma gas mixture effectively promotes the incorporation of Ne and Ar into the nanobubbles. In addition to the microstructural (SEM and TEM) and elemental composition (IBA) characterizations, also XAS and XPS spectroscopic studies were undertaken for Ne-charged Si films synthesized by MS with Ne and He-Ne gas mixtures. Our results were analyzed for the Ne K-edge excitation and 1s binding energies and discussed considering data previously reported for Ne and He bubbles obtained by ion implantation in aluminum [43,44] or martensitic steel [45]. Previous spectroscopic data were also obtained under conditions of cryo-condensation for He and Ne [44,46] or high-pressure devices for helium ([47] and references therein). New results are presented and discussed here for the gas-charged films fabricated by MS.

Based on the results presented in this article, the investigated Si films are thought of interest for the study of spectroscopic properties of condensed noble gases without the need of cryogenic, high-pressure anvils or ion implanter devices. The fabrication of these Ne and Ar solid targets are also of interest for nuclear reactions studies [28–33].

## 2. Materials and Methods

### 2.1. Films Preparation

Si films were prepared in a magnetron sputtering (MS) deposition chamber (residual vacuum in the range  $1 \times 10^{-6}$  mbar) operated with one magnetron head furnished with a 2 inch Si cathode placed at 30° towards the sample holder. The Si target was supplied from Neyco with 99,999 % purity. The distance from target to substrate was 5 cm vertically and the sample holder was rotated during deposition. As process gas we used He, Ne and Ar supplied by Air Liquid with 99,999 % purity. Table 1 summarizes the nomenclature of investigated samples along with their deposition parameters (gas pressures, power and time) and deposition rate (derived from film thickness measurements). Thin films were grown on 100 Si wafer substrates (0.5 mm thick) using a magnetron from the AJA (USA) Company. For operation power supplies from Cesar RF-Dressler and Advance Energy-Pinnacle Plus were respectively used in RF and DC mode with constant power. The sample holder is at floating potential and was not cooled during the process.

## 2.2. Films Characterization (Microstructure and Elemental Composition)

The thickness and morphology of the films were examined by scanning electron microscopy (SEM) employing a HITACHI S-4800 SEM-FEG microscope operated at 1-2 kV. The samples deposited on silicon substrates were cleaved for cross-sectional views. The nanostructure of the nanocomposite films was investigated at the Laboratory of Nanoscopies and Spectroscopies (LANE-ICMS, Sevilla, Spain) by Transmission Electron Microscopy (TEM) using a Jeol 2100Plus and a Tecnai G2 F30 TEM operated at 200 and 300 kV, respectively. The cross-sectional TEM lamellas were prepared by mechanical polishing and dimple grinding of the coatings deposited on silicon, followed by Ar<sup>+</sup> ion milling to electron transparency. Representative porous areas were selected for imaging and analysis. The pore distribution was evaluated from TEM micrographs by binarizing them and using the “Analyze Particle” function of ImageJ software [48].

Si, Ne, Ar and He content were derived from Ion Beam Analysis (IBA) carried out at the National Centre for Accelerators (CNA, Seville, Spain) using a 2.0 MeV proton beam and a passivated implanted planar-silicon (PIPS) detector set at 165°. Data analyses were performed by simulations with the SIMNRA code [49]. For the case of S1 and S2 samples, a complete IBA analysis including possible impurities (C, O, H) was additionally carried out at the SIAM platform of the University of Namur (Belgium) using a 2M-Tandetron Linear Accelerator from HVEE. Following conditions were used: i) With the alpha-beam, the samples were analyzed at 2.4 MeV in tilted incidence to determine the H content by ERD (elastic recoil detection). Then EBS (elastic backscattering spectrometry) spectra were collected from the same location at various incident energies, namely, at 3.05 MeV to determine the oxygen content [50], at 3.75 MeV to determine the nitrogen content [51], and at 4.3 MeV to determine the carbon content [52]. ii) The samples were then analyzed with a proton-beam at 1.96 MeV (p-EBS) for sensitivity to Ne and He. The set of 5 spectra acquired on each sample was self-consistently fitted with DataFurnace [53], using the stopping power provided by SRIM database (www.srim.org) as well as the evaluated cross-section functions available on the SigmaCalc [54], for extracting the elemental depth profiles.

## 2.3. Films Characterization (Spectroscopies Studies)

X-ray photoelectron spectroscopy (XPS) spectra were recorded with a SPECS electron spectrometer equipped with a PHOIBOS 150 hemispherical analyzer using Al K $\alpha$  radiation with 35 eV pass energy and normal emission take-off angle. The Si films deposited on silicon-wafer pieces were analyzed as received and after a gentle Ar sputtering (2.70 keV). The spectra were calibrated with the Si 2p signal at 99.2 eV.

X-Ray absorption spectroscopy (XAS) at the Ne K-edge was carried out at the beamline Antares of the Synchrotron Soleil (www.synchrotron-soleil.fr/en/beamlines/antares). Spectra were measured in the 855 to 900 eV photon range by fluorescence emission yields using a low energy fluorescence detector from Bruker.

## 3. Results and Discussion

### 3.1. Selection of Experimental Conditions for the Fabrication of Investigated Gas-Charged Silicon Films

Deposition conditions were selected aiming to elucidate the effect of helium incorporation in MS deposition of Si films when using Ne (or Ar) as process gas. Table 1 summarizes three selected cases of study for the case of Ne: i) Samples S1, S2 and S3 grown at 150 W in dc mode using pure Ne (S1) and two different Ne-He mixtures (S2 and S3). ii) Samples S4 and S5 grown at 150 W in rf mode using pure Ne (S4) and one Ne-He mixture (S5). iii) Samples S6 and S7 grown at 300 W in dc using pure Ne (S6) and one Ne-He mixture (S7). For the case of Ar two samples were fabricated at 150 W in dc mode using pure Ar (S8) and one Ar+He mixture (S9).



**Table 1.** Nomenclature and deposition parameters for investigated samples.

Sample nr. Description	Deposition time (h)	Sputtering gas and pressure (Pa)	Power (dc or rf) (W)	Deposition rate* (nm/min)
<b>S1:</b> Si-Ne/150dc/2Ne	2	2(Ne)	150 (dc)	12.6±0.4
<b>S2:</b> Si-Ne(He)/150dc/2Ne+2He	2	2(Ne)+2(He)	150 (dc)	12.1±0.3
<b>S3:</b> Si-Ne(He)/150dc/1Ne+1He	3	1(Ne)+1(He)	150 (dc)	11.9±0.3
<b>S4:</b> Si-Ne/150rf/2Ne	2	2(Ne)	150 (rf)	8.6±0.2
<b>S5:</b> Si-Ne(He)/150rf/2Ne+2He	3.5	2(Ne)+2(He)	150 (rf)	7.0±0.1
<b>S6:</b> Si-Ne/300dc/2Ne	1.5	2(Ne)	300 (dc)	31.5±0.5
<b>S7:</b> Si-Ne(He)/300dc/2Ne+2He	1.5	2(Ne)+2(He)	300 (dc)	24.6±0.4
<b>S8:</b> Si-Ar/150dc/2Ar	0.75	2(Ar)	150 (dc)	16.2±0.5
<b>S9:</b> Si-Ar(He)/150dc/1Ar+1He	1.25	1(Ar)+1(He)	150 (dc)	15.1±0.3

\*Calculated from deposition time and the thickness determined by SEM.

### 3.2. The Microstructure and Elemental Composition of Ne-Charged Silicon Thin Films

Figure 1 presents an overview of cross-section SEM images, obtained for the samples fabricated to investigate the Ne incorporation (samples 1 to 7 in Table 1). The images are grouped considering the three cases of study described above. A columnar structure is clearly observed for the samples grown in pure Ne (S1, S4, S6). When He is added to the deposition plasma (S2, S3, S5, S7) the observed features in the cross-section images are not relevant and correspond only to cleavage effects. Higher magnification SEM images for representative S4 and S5 samples are presented in Figure 2. The Si-Ne film (S4) shows the dense columnar microstructure while the Si-Ne(He) film (S5) shows the presence of nano porosity/nanobubbles. The thickness and column width ranges for the Si films were determined from the cross-section SEM images and are included in Table 2.

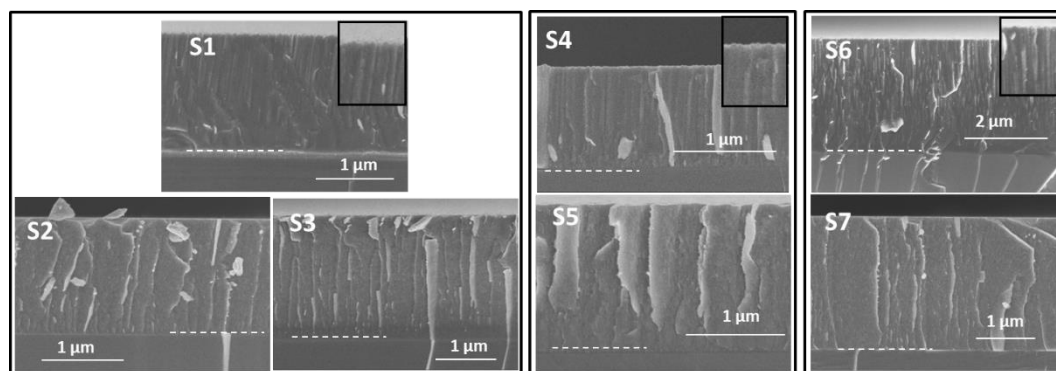


**Figure 1.** Cross-section SEM images of samples 1 to 7. Samples 1, 4 and 6 correspond to Si-Ne. Samples 2, 3, 5 and 7 correspond to Si-Ne(He). Notes: (i) Scales are not equal to visualize entire layers maximizing magnification. (ii) For the Si-Ne samples zoom images show columnar microstructure. (iii) Dash lines mark the interface between the silicon substrate and the coating.

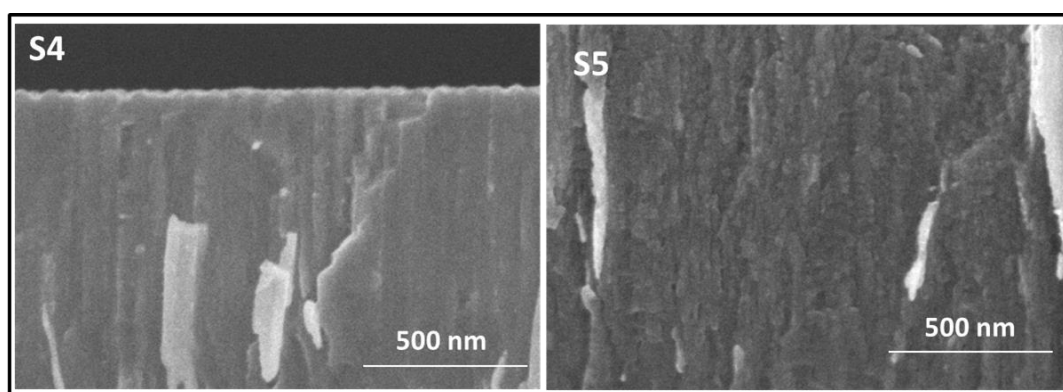


**Figure 2.** Cross-section SEM images at high magnification for representative S4(Ne) and S5(Ne+He) samples.

**Table 2.** SEM and TEM microstructural analysis of investigated samples.

Sample nr. Description	Thickness (SEM) ( $\mu\text{m}$ )	Column size range (SEM) (nm)	Mean column size (SEM) (nm)	Pore size range (TEM) (nm)	Mean pore size (TEM) (nm)	Mean aspect ratio (TEM)
S1: Si-Ne/150dc/2Ne	1.51 $\pm$ 0.02	30-115	64 $\pm$ 24	1-5	2.5 $\pm$ 0.9	0.6 $\pm$ 0.2
S2: Si-Ne(He)/150dc/2Ne+2He	1.45 $\pm$ 0.01			1-12	5.5 $\pm$ 2.3	0.6 $\pm$ 0.2
S3: Si-Ne(He)/150dc/1Ne+1He	2.14 $\pm$ 0.01					
S4: Si-Ne/150rf/2Ne	1.03 $\pm$ 0.01	30-120	55 $\pm$ 28	1-5	1.7 $\pm$ 0.6	0.6 $\pm$ 0.2
S5: Si-Ne(He)/150rf/2Ne+2He	1.47 $\pm$ 0.01			1-20	3.8 $\pm$ 1.8	0.6 $\pm$ 0.2
S6: Si-Ne/300dc/2Ne	2.84 $\pm$ 0.02	20-100	60 $\pm$ 27	0.5-5	2.7 $\pm$ 0.8	0.7 $\pm$ 0.2
S7: Si-Ne(He)/300dc/2Ne+2He	2.22 $\pm$ 0.01			1-14	5.2 $\pm$ 2.7	0.5 $\pm$ 0.2
S8: Si-Ar/150dc/2Ar	0.73 $\pm$ 0.01	20-90	38 $\pm$ 20			
S9: Si-Ar(He)/150dc/1Ar+1He	1.13 $\pm$ 0.01	20-100	49 $\pm$ 26			

For a further higher magnification study, images from cross-section TEM lamellas are presented in Figure 3. Samples grown in pure Ne show the formation of small nanopores. The addition of He to the deposition process leads to formation of bigger nanopores with broad size and aspect ratio distributions. Data analysis and corresponding histograms are presented in supporting information (Figures 1s, 2s and 3s) and summarized in Table 2. Note that the pore size is defined as the diameter of a circle equivalent in area to the one obtained for each pore in the TEM images. This allows comparison of pores with different elongated shapes. Additionally, the cross-section TEM analysis shows in some images the characteristic intercolumnar porosity for films S1 and S4 grown in pure Ne. These images are included in Supporting Information (Figure 4s).

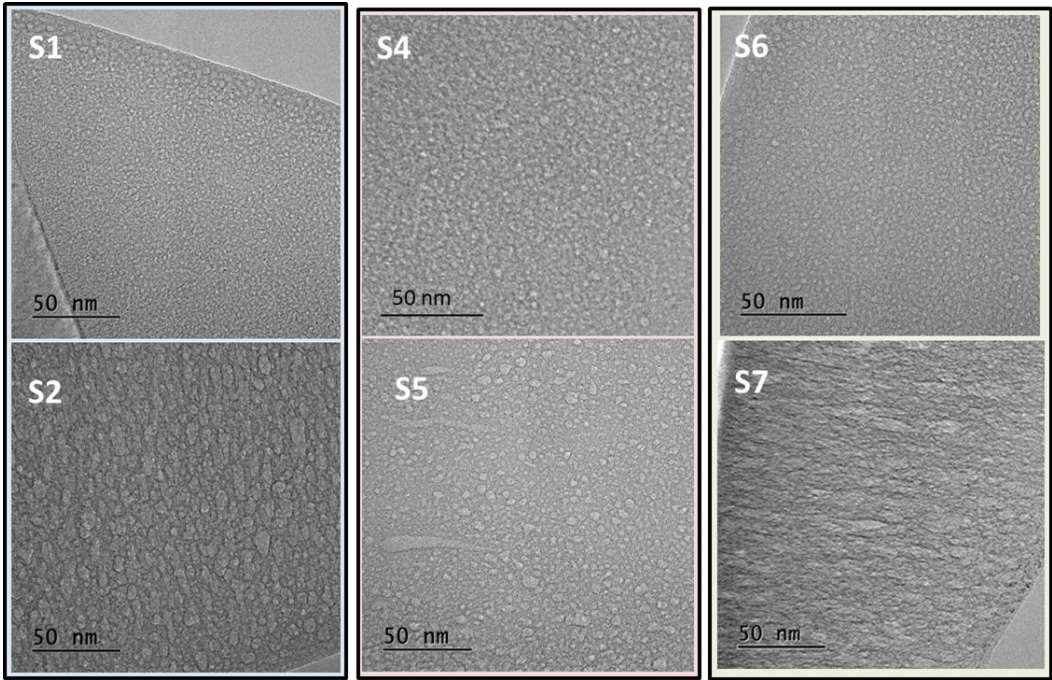


**Figure 3.** TEM cross-section images for representative samples: 1, 4 and 6 correspond to Si-Ne; 2, 5 and 7 correspond to Si-Ne(He).

Films composition were derived from IBA and are summarized in Tables 3 and 4. In this work an important advantage of this technique is the availability to quantify light elements as He and possible H, C and O contaminants. Impurities typically come from residual vacuum species activated during MS deposition [25]. Representative impurities are reported in Table 4 for samples S1 and S2. Figure 4 shows with bar diagrams the Ne/Si and He/Si atomic ratios obtained for the investigated samples associated to the selected cases of study. The addition of He is promoting the incorporation of Ne (and He) into the films together with the formation of numerous bigger and elongated nanopores as described above from the microstructural analysis. To illustrate this synergistic effect of He for Ne incorporation, Figure 5 presents the p-EBS spectra obtained for samples S1 and S2. The peaks due to scattering with He and Ne are clearly identified, evidencing the desired increase of Ne incorporation. The results in this section are therefore relevant in the contest of applications where the high amount of specific trapped gases is needed.

**Table 3.** Elemental composition for the investigated Si layers considering only main elements (Si, Ne, Ar and He).

Sample nr. Description	at% Si	at% Ne	at% Ar	at% He	Atomic ratio Ne/Si or Ar/Si	Atomic ratio He/Si
S1: Si-Ne/150dc/2Ne	94.1±2.3	5.90±0.25			0.063±0.004	
S2: Si-Ne(He)/150dc/2Ne+2He	71.8±1.8	10.95±0.50		17.24±0.90	0.15±0.01	0.24±0.02
S3: Si-Ne(He)/150dc/1Ne+1He	76.3±2.3	12.10±0.61		11.62±0.58	0.16±0.01	0.15±0.01
S4: Si-Ne/150rf/2Ne	89.5±2.7	10.5±0.53			0.12±0.01	
S5: Si-Ne(He)/150rf/2Ne+2He	66.9±2.0	13.0 ±0.65		20.1±1.0	0.19±0.01	0.30±0.02
S6: Si-Ne/300dc/2Ne	97.0±2.9	3.0±0.30			0.031±0.004	

S7: Si- Ne(He)/300dc/2Ne+2He	71.6±2.1	13.0±0.65	15.36±0.77	0.18±0.01	0.21±0.02
S8: Si-Ar/150dc/2Ar	99±1	1.00±0.15		0.010±0.001	
S9: Si- Ar(He)/150dc/1Ar+1He	89±10	4.8±0.3	5.7±0.5	0.05±0.01	0.06±0.01

Table 4. Elemental content for main contaminants in samples S1 and S2.

Sample nr. Description	at% C	at% O	at% H
S1: Si-Ne/150dc/2Ne	1.30±0.07	1.55±0.29	2.10±0.11
S2: Si-Ne(He)/150dc/2Ne+2He	1.22±0.08	2.85±0.38	2.74±0.27

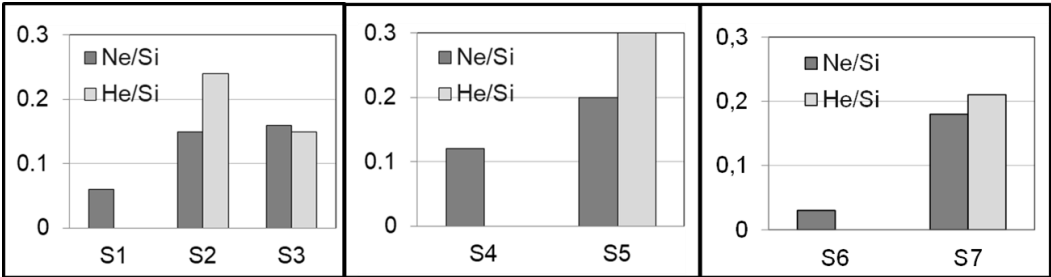


Figure 4. Bar diagram plots of atomic content ratio for the Si-Ne and Si-Ne(He) samples. For uncertainty values refer to Table 3.

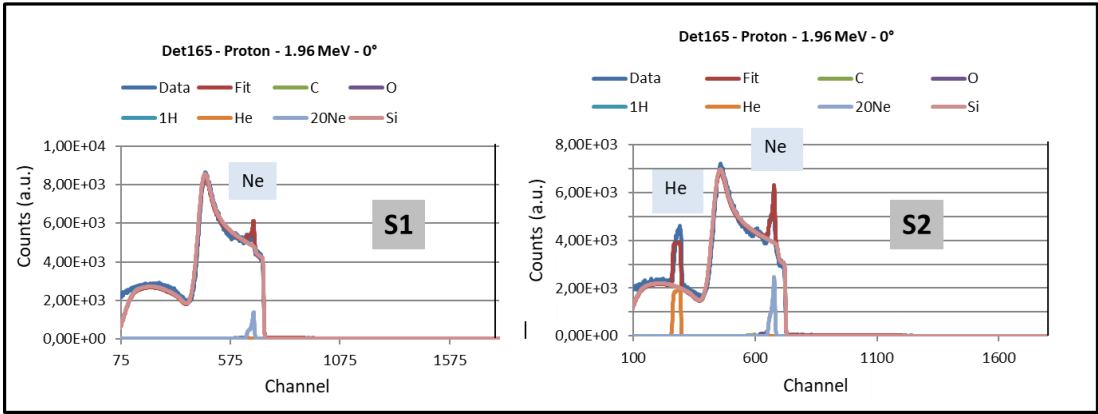


Figure 5. Proton beam EBS-spectra for representative samples: S1(Ne) and S2(Ne+He).

3.3. The Microstructure and Elemental Composition of Ar-Charged Silicon Thin Films

Figure 6 presents the cross-section SEM images obtained for the samples fabricated to investigate the Ar incorporation (samples 8 and 9 in Table 1). Both Si-Ar and Si-Ar(He) films show a columnar structure characteristic of Ar assisted MS deposition. Thicknesses and column width ranges for the Si films were determined from these cross-section SEM images and are included in Table 2. Figure 5s in supporting information includes additional top-view SEM images also showing the columnar microstructures. Consistent data about column sizes were found from these top-view SEM images (see Figure 5s). Note that due to the higher sputtering yield expected for Ar, shorter deposition times were used for samples S8 and S9. The prevalence of the columnar structure for the case of sample S9 is in agreement with the previously reported formation of Ar dominated plasmas during MS



deposition in Ar-He mixtures [15]. For a further higher magnification study, images from cross-section TEM lamellas are presented in Figure 7. Sample S8, grown in pure Ar, shows characteristic inter-columnar Ar trapped in defects while the addition of He leads to formation of larger intercolumnar gas accumulation. Data analysis regarding pore size and shape was not possible for these samples although an increase of intercolumnar porosity is clearly observed.

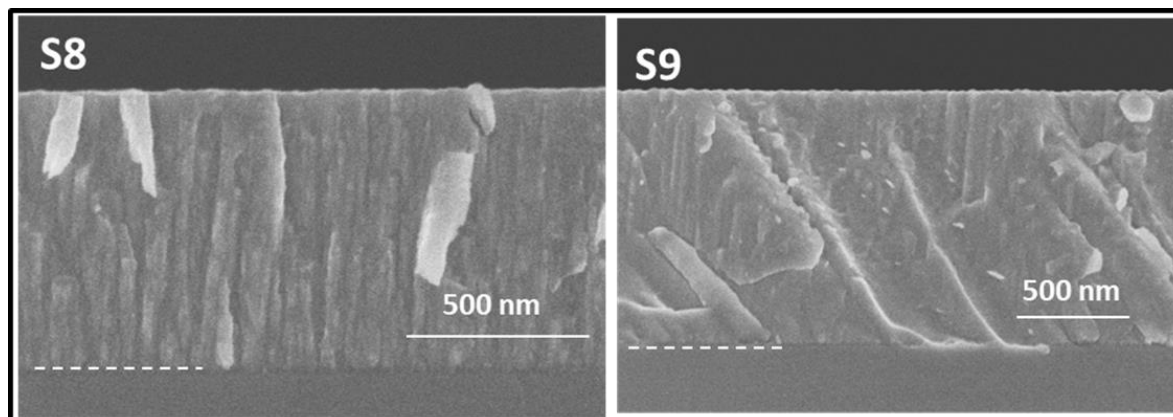


**Figure 6.** Cross-section SEM images for investigated S8(Ar) and S9(Ar+He) samples. Notes: (i) Scales are not equal to visualize entire layers maximizing magnification. (ii) Dash lines mark the interface between the silicon substrate and the coating.

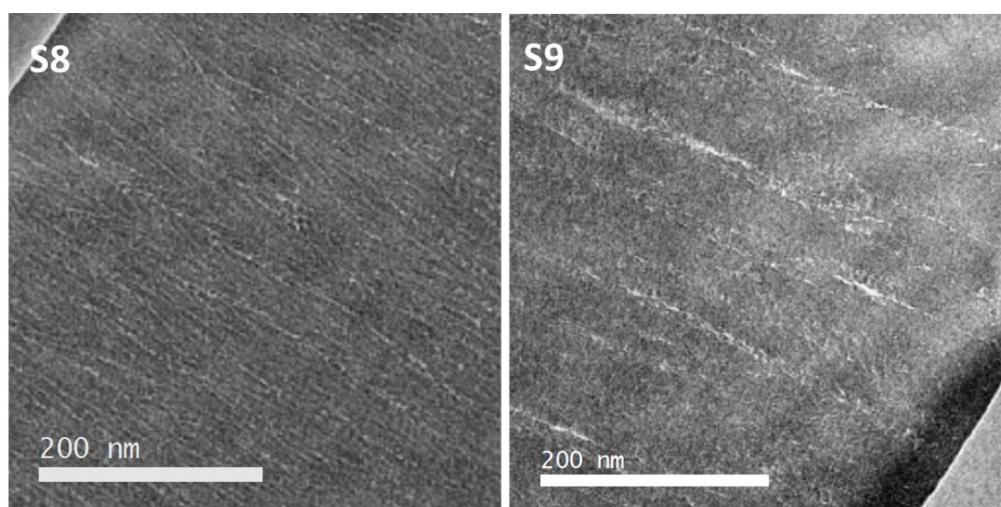


**Figure 7.** TEM cross-section images for the S8(Ar) and S9(Ar+He)) samples.

Films composition of main elements were derived from IBA and are summarized in Table 3. Although the Ar dominated plasma gave a similar columnar structure, and even if the amount of incorporated Ar is low (as compared to the Ne case), a synergistic effect was also found. Figure 8 shows with bar diagrams the obtained Ar/Si and He/Si atomic ratios for the two samples. The addition of He is promoting the Ar (and He) incorporation together with larger intercolumnar nanoporosity as described above from the microstructural analysis. Again, these results are relevant for applications where the high amount of specific trapped gases is needed.

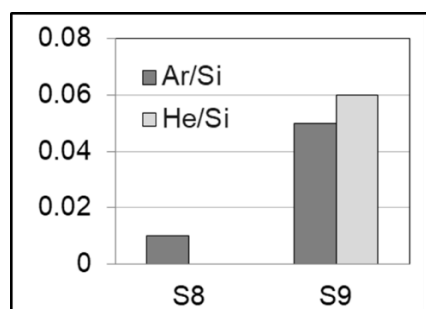


**Figure 8.** Bar diagram plots of atomic content ratios for the S8(Ar) and S9(Ar+He) samples. For uncertainty values refer to Table 3.

### 3.4. Spectroscopic Study of the Ne1s Binding Energy of Ne-Charged Si Films by XPS

Neon in the gas phase has a binding energy (Eb) for the 1s level of around 870-866 eV. When trapped in bubbles, typically in a metallic matrix as Al, it tends to shift to lower Eb [43]. The behavior is dominated by a final state effect associated to the screening of the photo-hole by the host-metal conduction electrons. The smaller the bubble, the greater the shift [43]. Similar results were also found for implanted Ar and Xe in respect to their gas phase Eb [10,55]. In this work samples S6 and S7 have been selected for the XPS study of the Ne K edge binding energy. Figure 9 shows the Ne1s photoelectron spectra for the as prepared samples showing the shift to lower Eb (~861.5 eV) for sample S6 (grown in pure Ne) with the smaller bubbles. The higher Ne 1s Eb (~862 eV) and the broader peak observed for the as prepared S7 sample is also in agreement with the larger mean pore size and the wider pore size distribution observed for this sample (5.2±2.7 nm) vs sample S6 (2.7±0.8 nm). See Figure 3s in supporting information. The increase of Ne 1s Eb after Ar sputtering in both samples may indicate that ion beam mixing effects could lead small bubbles to aggregate within larger bubbles.

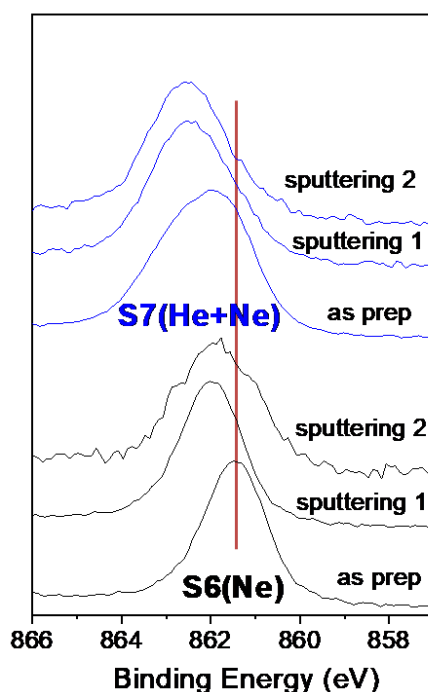


**Figure 9.** Bar diagram plots of atomic content ratios for the S8(Ar) and S9(Ar+He) samples. For uncertainty values refer to Table 3.

### 3.5. Spectroscopic Study of the Ne-Kedge Absorption Spectra of Ne-Charged Si Films by XAS

Previous characterizations of the He K-edge by Vacuum Ultraviolet absorption (VUV) [56] and Electron Energy Loss spectroscopy (EELS) [57] already demonstrated an absorption energy increase (in respect to the gas) for He condensed or encapsulated in bubbles. This behavior for the He  $1s \rightarrow 2p$  transition has been associated to the short-range Pauli pseudo-repulsion of the  $2p$ -electron wave function with the ground-state orbital of neighboring atoms [58,59]. This effect has also been measured at the microscopic scale monitoring individual bubbles in a transmission electron microscope by STEM-EELS [24,27,60]. For the case of gaseous Ne, the K-shell excitation has been also previously investigated by EELS spectroscopy using small-angle inelastic scattering of 2.5 keV electrons [61]. The relatively high amount of Ne incorporated in our Si films make us to consider the possibility to study the Ne K-edge in the films. Due to the low cross-section that we observed for the STEM-EELS analysis, X-ray Absorption Spectroscopy (XAS) measurements were done at the synchrotron Soleil facilities and are presented here. Previous studies of the K-shell excitation with X-ray photons have been also reported for condensed Ne films [62].

In this work samples S1-S2 and S6-S7 have been selected for the XAS study. The spectra in Figure 10 correspond to Ne-Kedge absorption for representative areas of investigated samples. In addition to the spectra, first derivative curves are also included in Figure 10 to determine inflection points (I.P.) of the absorption edges. According to EELS data for gaseous Ne reported in Ref. 61, a first absorption peak (I.P. at 860.0-860.5 eV) was assigned to the optically forbidden  $1s \rightarrow 3s$  electric quadrupole transition. It was followed by the allowed  $1s \rightarrow np$  absorption series (I.P. at 866.7 and 864.7 eV respectively for samples grown with Ne and Ne-He mixtures). In addition, results by X-ray photon absorption in Ref. 62, using different probes and experimental techniques, allowed one to selectively access the electronically excited states at the surface and inside the bulk of condensed solid Ne films. This work demonstrated, by using a surface selective probe, that the dipole forbidden  $1s \rightarrow 3s$  transition becomes allowed by admixture of  $3p_z$  character to the  $3s$  orbital due to asymmetric squeezing in the reduced symmetry of the surface layer [62]. This surface effect explains our observation with relatively high intensity of the first absorption peak for samples (S1 and S6) grown in pure Ne. The gas is trapped in numerous small pores (see Figures 3 and 3s) this maximizing the gas-matrix surface interaction at the pore-borders. The second peak for the allowed  $1s \rightarrow np$  series shows a shift towards higher absorption energy for samples S1 and S6 as expected for condensed Ne in the smaller bubbles.

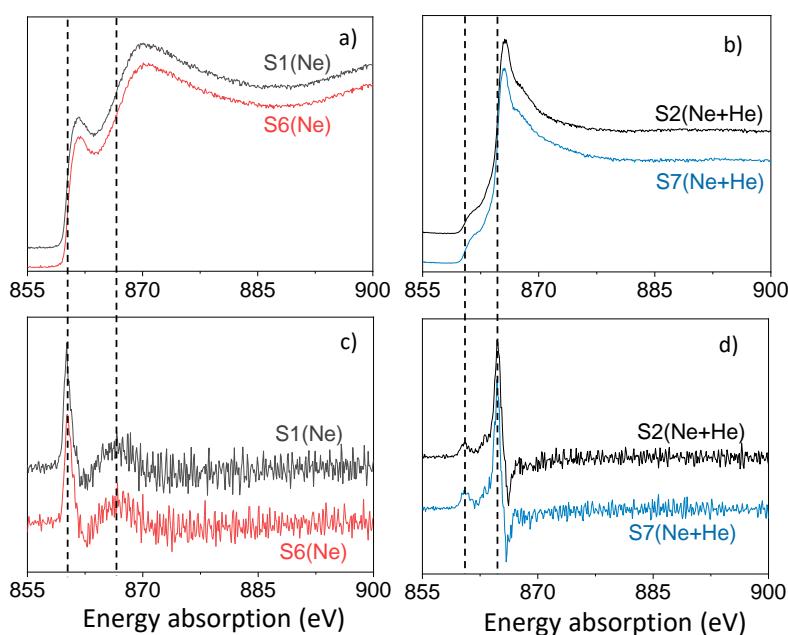


**Figure 10.** Normalized (a, b) and first derivative (c, d) of Ne 1s XAS spectra for samples S1(Ne), S2(Ne+He), S6(Ne) and S7(Ne+He).

#### 4. Conclusions and Perspectives

Previously we have investigated the production of He charged films by magnetron sputtering of silicon in pure He plasmas. In this work we show that the use of Ne or Ar as process gases leads to significantly lower gas incorporation as compared to He. An improved fabrication of Ne and Ar charged films is proposed in this work by synergistic effects when Ar-He or Ne-He gas mixtures are used. Ion Beam Analysis is a powerful tool to quantify the Ne, Ar and He contents within these solid-gas nanocomposite thin films. Microstructure and composition characterizations elucidated, not only the amounts of trapped gases, but also the effect of He addition on the size and shape distribution of bubbles associated to the trapped gases. Two effects can be concluded by adding He to the Ne or Ar MS deposition of silicon films: (i) He incorporation associated to increased Ne and Ar amounts; (ii) a larger mean pore size and a wider pore size distribution.

For the case of Ne charged silicon films spectroscopic studies were possible by XPS and XAS. The developed films are therefore of interest to characterize the spectroscopic properties of noble gases trapped in bubbles in a condensed state without the need of cryogenic devices or high-pressure anvils. Effects in the Ne 1s binding energy and K-edge absorption energies, both in XPS and XAS measurements, were respectively related to final (screening of the photo-hole) and initial (Pauli repulsions) state effects correlated to the pore size distributions. Density and pressure of the gas within the bubbles are relevant factors to be considered in future investigations. The results in this work are also important for applications of the “solid-gas” nanocomposite films as Ne (and Ar) solid targets for nuclear reaction experiments of interest in astrophysics and nuclear structure studies [28,29,32,33]. These solid targets can overcome limitations of cryogenic or gas cell-based systems, which are bulky and difficult to handle thus facilitating usage. As we have previously demonstrated for  $^3\text{He}$  [30,31] the methodology could also be extended in the future to the use of isotopes as  $^{21}\text{Ne}$ . A methodology to reduce the gas consumption for films fabrication is available [30,31].

**Supplementary Materials:** The following supporting information can be downloaded at the website of this paper posted on Preprints.org. Figure 1s: Study of samples S1 and S2. Pore (or trapped gas nanobubble) size and aspect ratio distribution histograms from TEM cross-sectional images, Figure 2s: Study of samples S4 and S5. Pore (or trapped gas nanobubble) size and aspect ratio distribution histograms from TEM cross-sectional images, Figure 3s: Study of samples S6 and S7. Pore (or trapped gas nanobubble) size and aspect ratio distribution histograms from TEM cross-sectional images, Figure 4s: TEM cross section images of samples S1 and S4, Figure 5s: SEM top-view images of samples S8 and S9.

**Author Contributions:** Conceptualization, A.F.; methodology and investigation, V.G., J.A., M.C.JdH, D.H., F.J.F., J.L.C., J.L.-V, G.E.A-V; M.C.A.; data curation, A.F., V.G., J.A., F.J.F., J.L.C.; writing—original draft preparation, A.F.; writing—review and editing, A.F., J.L.C.; supervision, A.F., S.L., M.C.A.; funding acquisition, A.F.S.L. All authors have read and agreed to the published version of the manuscript.

**Funding:** “This research was funded by the Spanish and Junta de Andalucía grants no. PID2021-124439NB-I00 and P20-00239 (both co-financed by EU FEDER) and the CSIC grant 202160E029. Authors thank SOLEIL beamtime allocation nr. 20170265. A.Fernández thanks the Spanish Ministry of Education for granting her with a visiting researcher fellowship (PRX-18/0052) at the Univ. Namur. F.J. Ferrer acknowledges the funding of the University of Seville through the grant VI PPIT-US.

**Data Availability Statement:** The data presented in this study are available on request from the corresponding author.

**Acknowledgments:** We also acknowledge the assistance of I. Rosa for the cross-section TEM lamellas preparation. The Synthesis, Irradiation and Analysis of Materials (SIAM) platform of Univ. Namur is acknowledged for IBA measurements.

**Conflicts of Interest:** The authors declare no conflicts of interest

#### References

1. Ullmaier, H. The influence of helium on the bulk properties of fusion reactor structural materials. *Nucl. Fusion* **1984**, *24*, 1039. [doi: 10.1088/0029-5515/24/8/009]
2. Lucas, A.A. Helium in metals. *Physica B+C* **1984**, *127*, 225–239.



3. Sun, X.; Chen, F.; Huang, H.; Lin, J.; Tang, X. Effects of interfaces on the helium bubble formation and radiation hardening of an austenitic stainless steel achieved by additive manufacturing. *Appl. Surf. Sci.* **2019**, *467–468*, 1134–1139. [doi: 10.1016/j.apsusc.2018.10.268]
4. Donnelly, S.E.; Evans, J.H. (eds). *Fundamental Aspects of Inert Gases in Solids*. Springer Science+Business Media New York © 1991. Originally published by Plenum Press, New York in 1991. [doi: 10.1007/978-1-4899-3680-6]
5. Gai, X.; Smith, R.; Kenny, S.D. Inert gas bubbles in bcc Fe. *J. Nucl. Mater.* **2016**, *470*, 84–89. [doi: 10.1016/j.jnucmat.2015.11.057]
6. Fleischer, E.L.; Norton, M.G. Noble gas inclusions in materials. *Heterog. Chem. Rev* **1996**, *3*, 171–201. [CCC: 1068-6983/96/030171-31]
7. Nishijima, Dai; Ye, M.Y.; Ohno, N.; Takamura, S. Formation mechanism of bubbles and holes on tungsten surface with low-energy and high-flux helium plasma irradiation in NAGDIS-II. *J. Nucl. Mater.* **2004**, *329–333*, 1029–1033. [doi: 10.1016/j.jnucmat.2004.04.129]
8. Pentecoste, L.; Brault, P.; Thomann, A.-L.; Desgardin, P.; Lecas, T.; Belhabib, T.; Barthe, M.-F.; Sauvage, T. Low energy and low fluence helium implantations in tungsten: Molecular dynamics simulations and experiments. *J. Nucl. Mater.* **2016**, *470*, 44–54. [doi: 10.1016/j.jnucmat.2015.12.017]
9. Oliviero, E.; Peripolli, S.; Fichtner, P.F.P.; Amaral, L. Characterization of neon implantation damage in silicon. *Materials Science and Engineering B* **2004**, *112*, 111–115. [doi: 10.1016/j.mseb.2004.05.014]
10. Biswas, C.; Shukla, A. K.; Banik, S.; Barman, S. R. Argon Nanobubbles in Al(111): A Photoemission Study. *Phys. Rev. Lett.* **2004**, *92*, 115506 (4 pp). [doi: 10.1103/PhysRevLett.92.115506]
11. Cummings, R. B.; Blackmur, M. S.; Grunwald M.; Minty A.; Styman, P.; MacLaren I. Xenon bubbles formed by ion implantation in zirconium alloy films. *J. Nucl. Mater.* **2022**, *560*, 153497 (7pp). [doi: 10.1016/j.jnucmat.2021.153497]
12. Eriksson, L.; Davies, J.A.; Mayer, J.W. Ion implantation studies in silicon, *Science* **1969**, *163*, 627–633. [doi: 10.1126/science.163.3868.627]
13. Nastasi, M.; Meyer, J.W. *Ion Implantation and Synthesis of Materials*; Springer Berlin: Heilderberg, Germany 2006. [doi: 10.1007/978-3-540-45298-0]
14. Sahu, B.B.; Kim, S.I.; Lee, M.W.; Han, J.G. Effect of helium incorporation on plasma parameters and characteristic properties of hydrogen free carbon films deposited using DC magnetron sputtering. *J. Appl. Phys.* **2020**, *127*, 014901 (9pp). [doi: 10.1063/1.5115449]
15. Ibrahim, S.; Zahrae Lahboub, F.; Brault, P.; Petit, A.; Caillard, A.; Millon, E.; Sauvage, T.; Fernández, A.; Thoman, A.-L. Influence of helium incorporation on growth process and properties of aluminum thin films deposited by DC magnetron sputtering. *Surf. Coat. Technol.* **2021**, *426*, 127808 (8pp). [doi: 10.1016/j.surfcoat.2021.127808]
16. Shi, L.Q.; Liu, C.Z.; Xu, S.L.; Zhou, Z.Y. Helium-charged titanium films deposited by direct current magnetron sputtering. *Thin Solid Films* **2005**, *479*, 52–58. [doi: 10.1016/j.tsf.2004.11.108]
17. Godinho, V.; Caballero-Hernández, J.; Jamon, D.; Rojas, T.C.; Schierholz, R.; García-López, J.; Ferrer, F. J.; Fernández, A. A new bottom-up methodology to produce silicon layers with a closed porosity nanostructure and reduced refractive index. *Nanotechnology* **2013**, *24*, 275604 (10pp). [doi: 10.1088/0957-4484/24/27/275604]
18. Liu, C.Z.; Shi, L.Q.; Zhou, Z.Y.; Hao, X.P.; Wang, B.Y.; Liu S.; Wang, L.B. Investigations of helium incorporated into a film deposited by magnetron sputtering. *J. Phys. D: Appl. Phys.* **2007**, *40*, 2150–2156. [doi: 10.1088/0022-3727/40/7/044]
19. Caballero-Hernández, J.; Godinho, V.; Lacroix, B.; Jiménez de Haro, M.C.; Jamon, D.; Fernández, A. Fabrication of Optical Multilayer Devices from Porous Silicon Coatings with Closed Porosity by Magnetron Sputtering. *ACS Appl. Mater. Interfaces* **2015**, *7*, 13889–13897. [doi: 10.1021/acsami.5b02356]
20. Sakabe, J.; Ohta, N.; Ohnishi, T.; Mitsuishi, K.; Takada, K. Porous amorphous silicon film anodes for high capacity and stable all-solid-state lithium batteries. *Commun. Chem.* **2018**, *1*, 24 (9pp). [doi: 10.1038/s42004-018-0026-y]
21. Uchida, G.; Nagai, K.; Habu, Y.; Hayashi, J.; Ikebe, Y.; Hiramatsu, M.; Narishige, R.; Itagaki, N.; Shiratani, M.; Setsuhara, Y. Nanostructured Ge and GeSn films by high-pressure He plasma sputtering for high-capacity Li ion battery anodes. *Sci. Rep.* **2022**, *12*, 1742 (11 pp). [doi: 10.1038/s41598-022-05579-z]
22. Ovejero, J.G.; Godinho, V.; Lacroix, B.; García, M. A.; Hernando, A.; Fernández, A. Exchange bias and two steps magnetization reversal in porous Co/CoO layers. *Mater. Des.* **2019**, *171*, 107691 (9pp). [doi: 10.1016/j.matdes.2019.107691]
23. Giarratano, F.; Arzac, G.M.; Godinho, V.; Hufschmidt, D.; Jiménez de Haro, M.C.; Montes, O.; Fernández, A. Nanoporous Pt-based catalysts prepared by chemical dealloying of magnetron-sputtered Pt-Cu thin

- films for the catalytic combustion of hydrogen. *Applied Catalysis B: Environmental* **2018**, 235, 168-176. [doi: 10.1016/j.apcatb.2018.04.064]
24. Schierholz, R.; Lacroix, B.; Godinho, V.; Caballero-Hernández, J.; Duchamp, M.; Fernández, A. STEM-EELS analysis reveals stable high density He in nanopores of amorphous silicon coatings deposited by magnetron sputtering. *Nanotechnology* **2015**, 26, 075703 (10pp). [doi: 10.1088/0957-4484/26/7/075703]
  25. Fernández, A.; Sauvage, T.; Diallo, B.; Hufschmidt, D.; Jiménez de Haro, M.C.; Montes, O.; Martínez-Blanes, J.M.; Caballero, J.; Godinho, V.; Ferrer, F.J.; Ibrahim, S.; Brault, P.; Thomann, A.-L. Microstructural characterization and thermal stability of He charged amorphous silicon films prepared by magnetron sputtering in helium. *Materials Chemistry and Physics* **2023**, 301, 127674 (11pp). [doi: 10.1016/j.matchemphys.2023.127674]
  26. Lacroix, B.; Godinho, V.; Fernández, A. The nanostructure of porous cobalt coatings deposited by magnetron sputtering in helium atmosphere. *Micron* **2018**, 108, 49–54. [doi: 10.1016/j.micron.2018.02.004]
  27. Pyper, N.C.; Thom, A.J.W.; Whelan, C.T. The density and pressure of helium nano-bubbles encapsulated in silicon. *Proc.R.Soc.A* **2023**, 479, 2023.0081. [doi: 10.1098/rspa.2023.0081]
  28. Godinho, V.; Ferrer, F.J.; Fernández, B.; Caballero-Hernández, J.; Gómez-Camacho, J.; Fernández, A. Characterization and Validation of a-Si Magnetron-Sputtered Thin Films as Solid He Targets with High Stability for Nuclear Reactions. *ACS Omega* **2016**, 1, 1229–1238. [doi: 10.1021/acsomega.6b00270]
  29. Carozzi, G.; Valiente-Dobón, J. J.; Gadea, A.; Siciliano, M.; Mengoni, D.; Fernández, A.; Godinho, V.; Hufschmidt, D.; Di Nitto, A. Test of a  $^3\text{He}$  target for transfer reactions in inverse kinematics. *Il Nuovo Cimento C* **2019**, 42, 94 (4 pp). [doi: 10.1393/ncc/i2019-19094-9]
  30. Fernández, A.; Hufschmidt, D.; Colaux, J.L.; Valiente-Dobón J.J.; Godinho, V.; Jiménez de Haro, M.C.; Fera, D.; Gadea, A.; Lucas, S. Low gas consumption fabrication of  $^3\text{He}$  solid targets for nuclear reactions. *Mater. Des.* **2020**, 186, 108337 (10pp). [doi: 10.1016/j.matdes.2019.108337]
  31. Fernández, A.; Hufschmidt, D.; Godinho, V.; Jiménez de Haro, M.C. Spanish patent application No. P201831107, Procedimiento de obtención de un material sólido con agregados gaseosos mediante pulverización catódica por magnetron en condiciones estáticas o cuasiestáticas para reducir el consumo de gas, patent filed on 15 Nov **2018**. [WO2020099695A1]
  32. Ferrer, F.J.; Fernández, B.; Fernández-García, J.P.; Barba, F.G.; Fernández, A.; Galaviz, D.; Godinho, V.; Gómez-Camacho, J.; Sánchez-Benítez, A.M. Novel solid  $^4\text{He}$  targets for experimental studies on nuclear reactions:  $^6\text{Li}+^4\text{He}$  differential cross-section measurement at incident energy of 5.5 MeV. *Eur. Phys. J. Plus* **2020**, 135, 465 (8pp). [doi: 10.1140/epjp/s13360-020-00482-w]
  33. Angus, C.; Williams, M.; et al. Measurement of the  $^{86}\text{Kr}(\alpha, n)^{89}\text{Sr}$  cross section at energies relevant for the weak r-process. *NPA-X 2022, EPJ Web of Conferences* **2023**, 279, 11003 (5pp). [doi: 10.1051/epjconf/202327911003]
  34. Depla, D.; Mahieu, S.; Greene, J.E. Handbook of Deposition Technologies for Films and Coatings (3rd edition). Chapter 5: Sputter Deposition Processes. *William Andrew Publishers* **2010**, pp: 253-296. [doi: 10.1016/B978-0-8155-2031-3.00005-3]
  35. Jacobsohn, L.G.; Averitt, R.D.; Nastasi, M. The role of trapped Ar atoms in the mechanical properties of boron carbide films deposited by dc-magnetron sputtering. *J. Vac. Sci. Technol. A* **2003**, 21, 1639–1643. [doi: 10.1116/1.1593054]
  36. Sagara, R.; Kawamura, M.; Kiba, T.; Abe, Y.; Kim, K.H. Characteristics of Ag thin films sputter deposited using Ar or Kr gas under different pressure. *Surf. Coat. Technol.* **2020**, 388, 125616 (4pp). [doi: 10.1016/j.surfcoat.2020.125616]
  37. Hatton, P.; Abbas, A.; Kaminski, P.; Yilmaz, S.; Watts, M.; Walls, M.; Goddard, P.; Smith, R. Inert gas bubble formation in magnetron sputtered thin-film CdTe solar cells. *Proc.R.Soc.A* **2020**, 476, 2020.0056. [doi: 10.1098/rspa.2020.0056]
  38. Godinho, V.; Moskovkin, P.; Álvarez, R.; Caballero-Hernández, J.; Schierholz, R.; Bera, B.; Demarche, J.; Palmero, A.; Fernández, A.; Lucas, S. On the formation of the porous structure in nanostructured a-Si coatings deposited by dc magnetron sputtering at oblique angles. *Nanotechnology* **2014**, 25, 355705 (11pp). [doi: 10.1088/0957-4484/25/35/355705]
  39. Petrov, I.; Ivanov, I.; Orlinov, V. Comparison of magnetron sputtering deposition conditions in neon, argon, krypton, and xenon discharges. *J. Vac. Sci. Technol. A* **1993**, 11, 2733-2741. [doi: 10.1116/1.578634]
  40. Wicher, B.; Chodun, R.; Greczynski, G.; Lackowski, A.; Trzcinski, M.; Pshyk, A.V.; Król, K.; Kulikowski, K.; Skowronski, L.; Zdunek, K. Carbon ion self-sputtering attained by sublimation of hot graphite target and controlled by pulse injection of a neon-helium gas mixture, *Appl. Surf. Sci.* **2023**, 620, 156708 (15pp). [doi: 10.1016/j.apsusc.2023.156708]

41. Aijaz, A.; Sarakinos, K.; Lundin, D.; Brenning, N.; Helmersson, U. A strategy for increased carbon ionization in magnetron sputtering discharges. *Diam. Relat. Mater* **2012**, *23*, 1–4. [doi: 10.1016/j.diamond.2011.12.043]
42. Tiron, V.; Bulai, G.; Costin, C.; Velicu, I.-L.; Dincă, P.; Iancu, D.; Burducea, I. Growth and characterization of W thin films with controlled Ne and Ar contents deposited by bipolar HiPIMS. *Nucl. Mater. & Energy* **2021**, *29*, 101091 (9pp). [doi: 10.1016/j.nme.2021.101091]
43. Dhaka, R.S.; Barman, S.R. Bimodal distribution of neon nanobubbles in aluminum. *Phys. Rev. B* **2009**, *79*, 125409 (6pp). [doi: 10.1103/PhysRevB.79.125409]
44. Lucas, A.A.; Vigneron J.P.; Donnelly, S.E.; Rife, J.C. Theoretical interpretation of the vacuum ultraviolet reflectance of liquid helium and of the absorption spectra of helium microbubbles in aluminium. *Phys. Rev. B* **1983**, *28*, 2485–2496. [doi: 10.1103/PhysRevB.28.2485]
45. Fréchar, S.; Walls, M.; Kociak, M.; Chevalier, J.P.; Henry, J.; Gorse D. Study by EELS of helium bubbles in a martensitic steel. *J. Nucl. Mater.* **2009**, *393*, 102–107. [doi: 10.1016/j.jnucmat.2009.05.011]
46. Romberg, R.; Kassühlke, B.; Wiethoff, P.; Menzel, D.; Feulner, P. Condensation effects in K-shell excitation and de-excitation of solid neon. *Chem. Phys.* **2003**, *289*, 69–79. [doi: 10.1016/S0301-0104(02)00901-1]
47. Arms, D.A.; Graber, T.J.; Macrander, A.T.; Simmons, R.O.; Schwoerer-Böhning, M.; Zhong, Y. Excitons in bulk liquid 4He. *Phys. Rev. B* **2005**, *71*, 233107. [doi: 10.1103/PhysRevB.71.233107]
48. W.S. Rasband, U. S. National Institutes of Health, Bethesda, Maryland, USA. ImageJ, available online: URL <https://imagej.nih.gov/ij/>.
49. Mayer, M. SIMNRA, a Simulation Program for the Analysis of NRA, RBS and ERDA. *AIP Conf. Proc.* **1999**, *475*, 541–544. [doi: 10.1063/1.59188]
50. Colaux, J.L.; Terwagne, G.; Jeynes, C. On the traceably accurate voltage calibration of electrostatic accelerators. *Nucl. Instrum. Methods Phys. Res. B* **2015**, *349*, 173–183. [doi: 10.1016/j.nimb.2015.02.048]
51. Gurbich, A.F.; Bogdanović Radović, I.; Siketić, Z.; Jakšić M. Measurements and evaluation of the cross-section for helium elastic scattering from nitrogen. *Nucl. Instrum. Methods Phys. Res. B* **2011**, *269*, 40–44. [doi: 10.1016/j.nimb.2010.10.007]
52. Gai, E.V.; Gurbich, A.F. Evaluated  $^{12}\text{C}(4\text{He},4\text{He})^{12}\text{C}$  cross-section and its uncertainty. *Nucl. Instrum. Methods Phys. Res. B* **2013**, *296*, 87–91. [doi: 10.1016/j.nimb.2012.12.006]
53. Barradas, N.P.; Jeynes, C.; Webb, R.P. Simulated annealing analysis of Rutherford backscattering data. *Appl. Phys. Lett.* **1997**, *71*, 291–293. [doi: 10.1063/1.119524]
54. Gurbich, A.F. SigmaCalc recent development and present status of the evaluated cross-sections for IBA. *Nucl. Instrum. Methods Phys. Res. B* **2016**, *371*, 27–32. [doi: 10.1016/j.nimb.2015.09.035]
55. Dhaka, R.S.; Biswas, C.; Shukla, A.K.; Barman, S.R.; Chakrabarti, A. Xe and Ar nanobubbles in Al studied by photoemission spectroscopy. *Phys. Rev. B* **2008**, *77*, 104119 (12 pp.). [doi: 10.1103/PhysRevB.77.104119]
56. Donnelly, S.E.; Rife, J.C.; Gilles, J.M.; Lucas, A.A. Optical measurements of the density of helium in small bubbles in aluminium films. *J. Nuc. Matter* **1980**, *93-94*, 767–772. [doi: 10.1016/0022-3115(80)90205-6]
57. Jäger, W.; Manzke, R.; Trinkhaus, H.; Crecelius, G.; Zeller, R.; Fink, J.; Bay, H.L. Density and pressure of helium in small bubbles in metals. *J. Nuc. Matter* **1982**, *111-112*, 674–680. [doi: 10.1016/0022-3115(82)90288-4]
58. Pyper, N.C.; Naginey, T.C.; Nellist, P.N.; Whelan, C.T. Excited helium under high pressures in the bulk and in nanobubbles. *Phil. Mag. Lett.* **2017**, *97*, 295–303. [doi: 10.1080/09500839.2017.1347724]
59. Pyper, N.C.; Naginey, T.C.; Whelan, C.T. Environmental modifications of atomic properties: The ground and 1s2p excited states of compressed helium. *J. Chem. Phys.* **2021**, *155*, 214301 (14 pp). [doi: 10.1063/5.0066626]
60. David, M.-L.; Pailloux, F.; Mauchamp, V.; Pizzagalli, L. In situ probing of helium desorption from individual nanobubbles under electron irradiation. *Appl. Phys. Lett.* **2011**, *98*, 171903 (3 pp). [doi: 10.1063/1.3582612]
61. Hitchcock, A.P.; Brion, C.E. Neon K-shell excitation by electron energy-loss spectroscopy. *J. Phys. B: Atom. Molec. Phys.* **1980**, *113*, 3269–3273. [doi: 10.1088/0022-3700/13/16/023]
62. Romberg, R.; Kassühlke, B.; Wiethoff, P.; Menzel, D.; Feulner, P. Condensation effects in K-shell excitation and de-excitation of solid neon. *Chem. Phys.* **2003**, *289*, 69–79. [doi: 10.1016/S0301-0104(02)00901-1]

**Disclaimer/Publisher's Note:** The statements, opinions and data contained in all publications are solely those of the individual author(s) and contributor(s) and not of MDPI and/or the editor(s). MDPI and/or the editor(s) disclaim responsibility for any injury to people or property resulting from any ideas, methods, instructions or products referred to in the content.